Desalination and Water Treatment
www.deswater.com

doi: 10.5004/dwt.2022.29115

280 (2022) 338–347
December

Tartaric acid-assisted combustion preparation of Y-doped ZnO nanoparticles used for highly efficient visible-light-driven photocatalyst

Anukorn Phuruangrat[a,*], Phittawas Sittiangkul[a], Titipun Thongtem[b,c], Somchai Thongtem[b,d,*]

[a]*Division of Physical Science, Faculty of Science, Prince of Songkla University, Hat Yai, Songkhla 90112, Thailand, Tel.: +66 (0)74 288374; Fax: +66 (0)74 288395; emails: phuruangrat@hotmail.com (A. Phuruangrat), 5910210228@psu.ac.th (P. Sittiangkul)*
[b]*Materials Science Research Center, Faculty of Science, Chiang Mai University, Chiang Mai 50200, Thailand, Tel.: +66 (0)53 941915; Fax. +66 (0)53 941915; emails: schthongtem@yahoo.com (S. Thongtem), ttpthongtem@yahoo.com (T. Thongtem)*
[c]*Department of Chemistry, Faculty of Science, Chiang Mai University, Chiang Mai 50200, Thailand*
[d]*Department of Physics and Materials Science, Faculty of Science, Chiang Mai University, Chiang Mai 50200, Thailand*

Received 9 January 2022; Accepted 4 November 2022

ABSTRACT

Y-doped ZnO nanoparticles as a visible-light-driven photocatalyst were successfully synthesized by a tartaric acid-assisted combustion method. The as-synthesized ZnO nanoparticles with and without Y dopant were characterized by X-ray diffraction, transmission electron microscopy, Raman spectroscopy, Fourier-transform infrared spectroscopy, X-ray photoelectron spectroscopy and UV-Visible spectroscopy. ZnO with and without Y dopant can be indexed to pure phase of hexagonal wurtzite ZnO nanoparticles. The particle size of ZnO was decreased after being doped with Y. The average nanoparticles were 72.91 ± 24.68 nm, 24.05 ± 7.24 nm, 21.83 ± 4.90 nm and 21.55 ± 3.81 nm for pure ZnO, 1% Y-doped ZnO, 3% Y-doped ZnO and 5% Y-doped ZnO, respectively. The maximum absorption of Y-doped ZnO was red-shift because of the formation of shallow level inside band gap caused by impurities containing in ZnO lattice. The activity of as-synthesized samples was evaluated based on the photodegradation of methylene blue (MB) under visible light irradiation. In this research, 3% Y-doped ZnO nanoparticles exhibited the highest efficiency of 97.19% within 100 min. $^{\bullet}OH$ and $^{\bullet}O_2^-$ radicals are main active species for MB degradation over Y-doped ZnO nanoparticles under visible light irradiation. The recycled test of 3% Y-doped ZnO nanoparticles was proved that 3% Y-doped ZnO nanoparticles are excellent photo-corrosion resistance and have stability for practical application under visible light irradiation.

Keywords: Tartaric acid-assisted combustion; Y-doped ZnO nanoparticles; Photocatalysis; Spectroscopy

1. Introduction

Zinc oxide as an n-type semiconductor with wide band gap energy (3.37 eV) and high excitonic binding energy (~ 60 meV) is one of the most promising semiconductor materials in the field of optoelectronic devices and solar energy conversion because it has excellent properties such as environmental material, high redox potential, low cost and high physical and chemical stability [1–4]. ZnO is an efficient photocatalyst in the degradation of numerous organic pollutants such as nitric oxide [1], orange G (OG) [2], methylene blue (MB) [3–6], rhodamine B (RhB) [4,7,8],

* Corresponding authors.

methyl orange (MO) [9,10] and chlorophenols [11] containing in water and air. It has high efficiency and mobility of photo-induced charge carriers [4,12,13]. Moreover, the photocatalytic application of ZnO is limited by high rate of photogenerated electron–hole pair recombination and it is active in only UV radiation [9,11,14]. To solve this problem, rare earth metal doped in ZnO lattice acts as an electron acceptor to suppress the recombination of photogenerated electron–hole pairs. It is responsive with visible light by producing impurity level within band gap, and the visible-light-driven photocatalytic reaction of ZnO is enhanced [2,4–6,9].

ZnO nanoparticles can be synthesized by different techniques such as sol–gel [1,9,11], co-precipitation [3,4,6], hydrothermal reaction [7,13,14], combustion [15–17] and microwave-assisted solution synthesis [18,19]. Among the various synthetic methods, combustion as exothermic redox reaction has some advantages over others. This method is used for large scale production because it has the utilization of heat release from combustion of metal nitrate acted as conventional oxidant and oxidation reaction of hydrocarbon species as fuel which can lead to release an enormous amount of heat [15,20–22]. Tartaric acid as a fuel was commonly used in the synthesis of metal oxide nanoparticles because carboxyl groups of tartaric acid are required for the formation of metal ion complexes to obtain homogeneous polyester precursor whereas hydroxyl groups are necessary for subsequent polyesterification of carboxyl groups, resulting to the pure phase, size distribution and crystallinity of the products at a given calcination temperature [15,20,22,23].

In this work, a series of Y-doped ZnO nanoparticles were synthesized by tartaric acid assisted combustion method. The prepared samples were characterized for phase, morphology and optical property. The photocatalytic performance of as-synthesized Y-doped ZnO nanoparticles was evaluated through the degradation of methylene blue (MB) under visible light irradiation. The trapping experiment was also studied to investigate the photocatalytic activity.

2. Experimental procedure

0.01 mol $Zn(NO_3)_2{\cdot}6H_2O$ and 0–5 wt.% $Y(NO_3)_3{\cdot}6H_2O$ were weighted and dissolved in 50 mL C_2H_5OH solutions at room temperature. The two dissolved solutions were mixed under continued magnetic stirring. Subsequently, 0.010 mol tartaric acid and 0.001 mol NaOH were weighted and dissolved in 50 mL C_2H_5OH at room temperature. Then, tartaric acid and NaOH solutions were also added to the mixed solution under continued magnetic stirring to form precipitates. In the end, the precipitates were filtered, washed with distilled water and ethanol, and dried in an electric oven at 80°C for 24 h. The dried precipitates were calcined in an electric furnace with a heating rate of 10°C/min at 600°C for 2 h.

Thermal analysis of dried gel was analyzed by thermogravimetric analysis (STA 8000 Simultaneous Thermal Analyzer (TGA), PerkinElmer) in nitrogen atmosphere with 10°C/min heating rate at T_R-800°C. The phase of products was characterized by X-ray diffraction (XRD) on a Philips X'Pert-MPD X-ray diffractometer equipped with Cu-K_α radiation ranging from 10° to 80° at a scanning rate of 0.005 deg/s. The morphology and elemental component were characterized by transmission electron microscopy (TEM) and selected area electron diffraction (SAED) taken on a JEOL JEM 2010 TEM with an acceleration voltage of 200 kV. Fourier-transform infrared spectroscopy (FTIR) of samples were analyzed by a Bruker Tensor 27 FTIR spectrometer at 400–4,000 cm^{-1} with 4 cm^{-1} resolution. Raman spectra of samples were analyzed by a Horiba Jobin Yvon T64000 Raman spectrometer with 514.5 nm wavelength Ar green laser. The surface and oxidation state of elements of sample were analyzed by Axis Ultra DLD|Kratos–Kratos Analytical X-ray photoelectron spectroscopy (XPS) using monochromated Al K_α radiation (1,486.6 eV) as a providing source and using the C 1s electron peak at 285.0 eV as a standard. The optical properties of samples were studied by a PerkinElmer Lambda 25 UV-Visible spectrometer at room temperature.

The photocatalytic activities of ZnO with and without Y dopant were monitored through methylene blue (MB) degradation under visible light irradiation. Each 200 mg of ZnO with and without Y dopant was weighted and added in 200 mL 10^{-5} M MB aqueous solutions which were magnetically stirred in the dark for 30 min. Then visible light irradiation from 35 W xenon lamp was turned on and the suspension solution was collected every 20 min interval for 100 min. The concentration of MB after photocatalytic reaction was analyzed by UV-Visible spectroscopy (PerkinElmer Lambda 25 UV-Visible spectrometer) at 664 nm wavelength. The decolorization efficiency (%) was calculated by:

$$\text{Decolorization efficiency}(\%) = \frac{C_0 - C_t}{C_0} \times 100 \quad (1)$$

where C_o and C_t are the concentrations of MB before and after visible light irradiation.

3. Results and discussion

A suitable calcination temperature of precursor was analyzed by thermogravimetric analysis (TGA) and differential thermal analysis (DTA) at T_R-800°C at a heating rate of 10°C/min in nitrogen atmosphere with a flowing rate of 50 mL/min as the results shown in Fig. 1. The TGA curve of precursor shows two steps of weight loss at T_R-226°C and 226°C–542°C while the DTA curve of precursor shows an exothermic peak between 310°C–373°C with a maximum peak at 324°C. The first weight loss of precursor at T_R-226°C is about 8.70% which is assigned to the loss of residual water containing in the precursor [15,17,20,21,24]. The second TGA step of precursor at 226°C–542°C shows the rapid decomposition process with weight loss of 55.54% due to the decomposition of hydrocarbon, carboxylic group of tartaric precursor and NO_3^- residue, including the transformation of precursor to crystalline product [15,17,20,21,24]. The process is associated with the exothermic peak at 324°C in DTA graph due to the pyrolysis process by transforming metal- tartaric acid precursor into crystalline ZnO structure [17,22,24]. Above 542°C, the weight of precursor was no longer decreased. Thus, the suitable calcination temperature of precursor is 600°C in this research.

XRD patterns of ZnO with and without different weight contents of Y are shown in Fig. 2. The XRD pattern of pure ZnO sample shows nine diffraction peaks at 31.83°, 34.58°,

36.31°, 47.56°, 56.13°, 62.97°, 66.53°, 67.98° and 69.13° which can be indexed to (100), (002), (101), (102), (110), (103), (200), (112) and (201) crystal planes of hexagonal wurtzite ZnO structure in agreement with the JCPDS No. 36-1451, respectively [25]. When Y was doped in ZnO samples, they showed nine diffraction peaks at almost the same diffraction angles as those of pure ZnO sample. The 5% Y-doped ZnO sample showed the diffraction peaks located at 31.73°, 34.36°, 36.30°, 47.54°, 56.56°, 62.94°, 66.54°, 67.93° and 69.04° for the (100), (002), (101), (102), (110), (103), (200), (112) and (201) crystal planes of hexagonal wurtzite ZnO structure (JCPDS No. 36-1451 [25]), respectively. The results indicated that Y^{3+} ions were uniformly distributed across the ZnO crystal lattice [2,5,6,9]. Clearly, three main diffraction peaks of Y-doped ZnO (Fig. 2b) showed the slight shift to lower diffraction angle because the ionic radius of Y^{3+} ion (1.019 Å [26–28]) is larger than the ionic radius of Zn^{2+} ion (0.74 Å [6,9,29,30]). Possibly, doped Y^{3+} ions were mainly substituted for regular Zn^{2+} lattice sites during combustion reaction [2,6,31]. Other phases such as Y_2O_3 and other impurities were not detected in these doped samples. The calculated unit cells of samples were a = 3.2436 Å and c = 5.1834 Å for ZnO and a = 3.2536 Å and c = 5.2156 Å for 5% Y-doped ZnO [2,4,6,9,32]. Thus, the unit cell of ZnO was enlarged after being doped with Y due to the lattice dislocation occurring in hexagonal ZnO lattice [2,6,32]. They should be noted that the intensities of diffraction peaks of Y-doped ZnO were decreased with the increase of weight content of Y. Thus, the degree of crystallinity and crystallite size of the samples were decreased by the doped Y which was the redistribution and rearrangement of surface atoms and alteration of surface bonds occurring inside [2,32]. The crystallite sizes of samples were calculated by the below Scherrer equation.

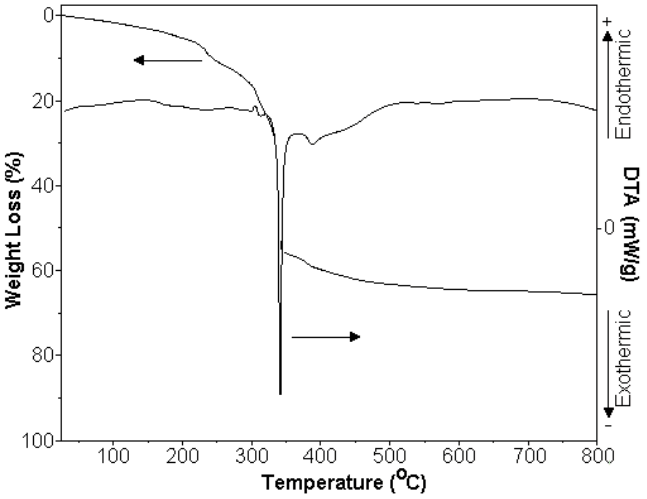

Fig. 1. TGA and DTA graphs of Zn-tartaric acid precursor with 5% Y dopant at T_R-800°C in nitrogen atmosphere.

$$D = \frac{K\lambda}{\beta\cos\theta} \quad (2)$$

where D is the crystallite size, K is the dimensionless shape factor with a value close to unity, β is the full width at half maximum and θ is the diffraction angle of the (101) crystal plane and λ is the wavelength of Cu K_α (1.54056 Å) [3,4,6,15,17]. The calculated crystallite sizes of samples were 38, 30, 26 and 24 nm for 0%, 1%, 3% and 5% Y-doped ZnO samples, respectively.

Wurtzite ZnO has hexagonal structure and belongs to the C^4_{6v} space group with eight types of optical modes located at the middle (Γ point) of Brillouin zone: $\Gamma = 1A_1 + 2B_1 + 1E_1 + 2E_2$ where A_1 and E_1 belong to two polar branches [15,19,33,34]. In case of nonpolar E_2, modes

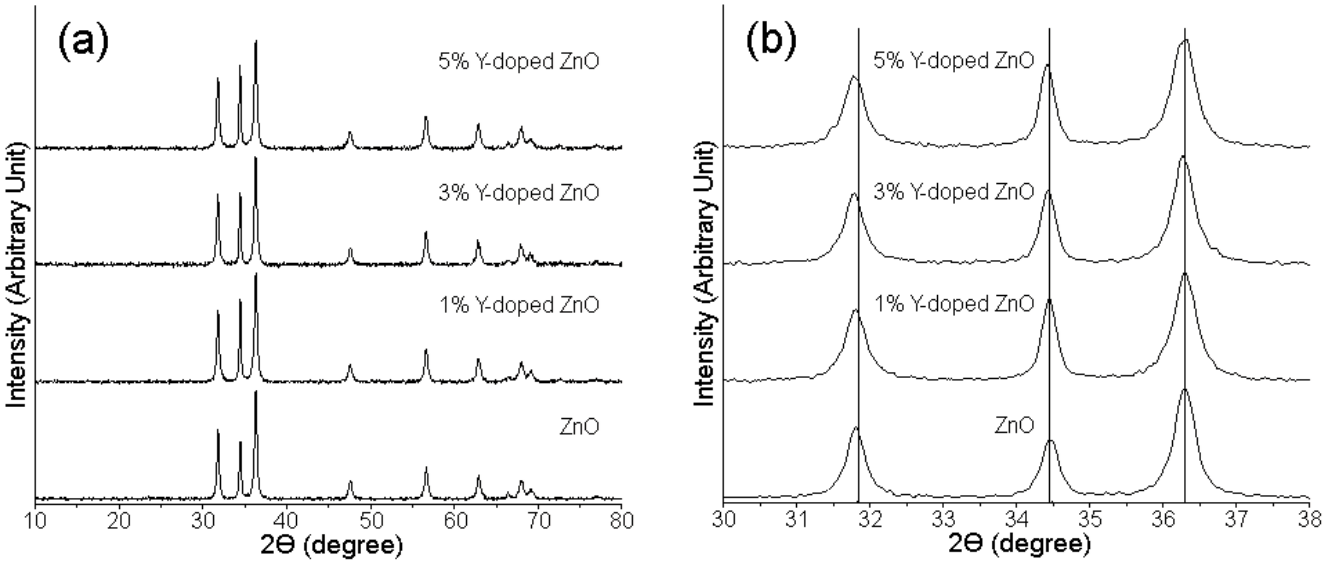

Fig. 2. XRD patterns of 0%–5% Y-doped ZnO samples synthesized by a tartaric acid-assisted combustion method over the 2θ range of (a) 10°–80° and (b) 30°–38°.

of low frequency (E_{2L}) are assigned to the Zn sub-lattice [15,19,33,34]. The other case, only oxygen atoms involve with high frequency mode (E_{2H}) [15,19,33,34]. The inactive B_1 mode is silent [15,19,33,34]. Fig. 3a shows the Raman spectra of the ZnO and 5% Y-doped ZnO samples at 200–800 cm^{-1} at room temperature. Raman spectrum of ZnO without Y dopant shows peaks located at 335, 379, 404, 438, and 535 cm^{-1}. The dominant Raman peak of ZnO without Y dopant at 438 cm^{-1} corresponds to the $E_{2(high)}$ mode of wurtzite ZnO structure [13,15,19,33–35]. The low intensity peaks observed around 335 and 379 cm^{-1} are attributed to the second-order Raman spectrum arising from zone-boundary phonons $E_{2(high)}$–$E_{2(low)}$ and $A_{1(TO)}$ modes of wurtzite ZnO structure [13,15,19,33–35]. The weak Raman peak at 535 cm^{-1} can be assigned to $E_{1(LO)}$ relating to the oxygen lattice distortion and defect in ZnO lattice such as oxygen vacancies (V_O) and zinc interstitials (Zn_i) [13,15,19,33–35]. They can be seen that the Raman spectrum of 5% Y-doped ZnO sample corresponds well to those of ZnO without Y dopant. Moreover, the Raman peak at 438 cm^{-1} of 5% Y-doped ZnO was broadened owing to the disorder of ZnO lattice. It can be seen that the Raman peaks at about 500–700 cm^{-1} of Y-doped ZnO samples become stronger which ascribed to the local vibrational mode of Y^{3+} substituted for Zn^{2+} in ZnO lattice and oxygen vacancies induced inside [29,34].

Fig. 3b shows FTIR spectra of ZnO and 5% Y-doped ZnO samples synthesized by combustion method. The FTIR spectrum of pure ZnO sample shows the sharp band at 427 cm^{-1} related to the stretching mode of Zn–O [3,6,13,15,19,29,36]. The FTIR spectrum of 5% Y-doped ZnO sample was blue shift to 434 cm^{-1} due to the change of bond length upon the substitution of Y^{3+} for Zn^{2+}. The results certified that Y ions were successfully incorporated in ZnO crystal structure [3,6,29,36–38].

The oxidation state of element containing in 3% Y-doped ZnO sample was analyzed by XPS (Fig. 4) using C 1s peak at 285.0 eV as the reference for calibration of binding energy. XPS survey spectrum of 3% Y-doped ZnO sample (Fig. 4a) was detected only the Y, Zn and O elements. Other elements were not detected in XPS analysis, indicating that the sample is very pure. Fig. 4b shows the XPS spectrum of Y 3d core level of 3% Y-doped ZnO. The sample shows four binding energy peaks at 156.83 and 158.05 eV for Y $3d_{5/2}$ and 158.70 and 160.40 eV for Y $3d_{3/2}$, suggesting the formation of Y–O and Y–OH bonds in ZnO lattice because Y^{3+} ions were incorporated in the ZnO lattice [39–42]. The two symmetric binding energies of Zn 2p core level (Fig. 4c) shows the strong peaks at 1,021.17 and 1,044.29 eV for 3% Y-doped ZnO sample corresponding to Zn $2p_{3/2}$ and Zn $2p_{1/2}$ orbitals. The orbital splitting of Zn 2p core level is 23.12 eV. Thus, the oxidation state of 3% Y-doped ZnO is divalent [6,9,16,32]. The asymmetric binding energy of O 1s core level (Fig. 4d) was de-convoluted into three peaks at 530.11, 531.49 and 532.40 eV for 3% Y-doped ZnO sample corresponding to Zn–O bond, oxygen vacancy and chemisorbed oxygen species, respectively. It can be seen that strong oxygen defect containing in 3% Y-doped ZnO sample act as a sink for photo-induced electron and hole, which can lead to enhance photocatalytic activity of Y-doped ZnO [6,9,16,32].

The morphologies of ZnO and Y-doped ZnO were observed by TEM as the results shown in Fig. 5. In this research, all samples were composed of spherical nanoparticles with different particle sizes. The particle size of sample was decreased with increasing in the concentration of Y dopant. The average and standard deviation of ZnO and Y-doped ZnO nanoparticles were 72.91 ± 24.68 nm, 24.05 ± 7.24 nm, 21.83 ± 4.90 nm and 21.55 ± 3.81 nm for pure ZnO, 1% Y-doped ZnO, 3% Y-doped ZnO and 5% Y-doped ZnO, respectively. The selected area electron diffraction patterns of ZnO and Y-doped ZnO samples inserted in Fig. 5 shows bright continuous concentric rings of diffraction electron spots, indicating that all samples were well polycrystal. They can be indexed to the (100), (002), (101), (102) and (110) planes of hexagonal ZnO structure in accordance with the above XRD analysis.

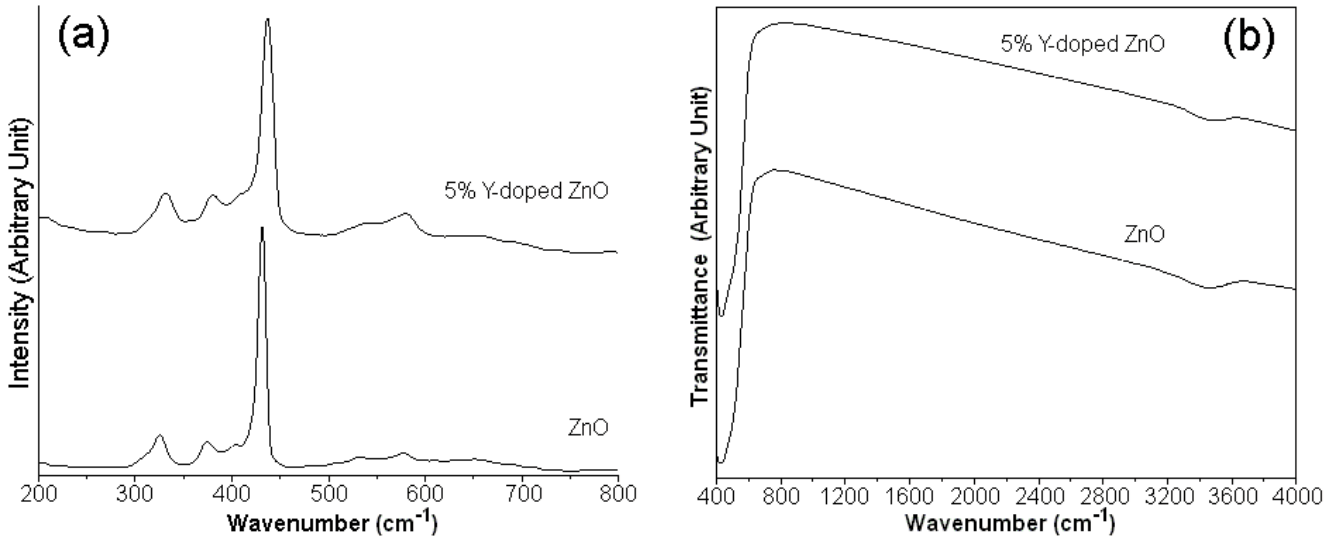

Fig. 3. (a) Raman and (b) FTIR spectra of pure ZnO and 5% Y-doped ZnO samples.

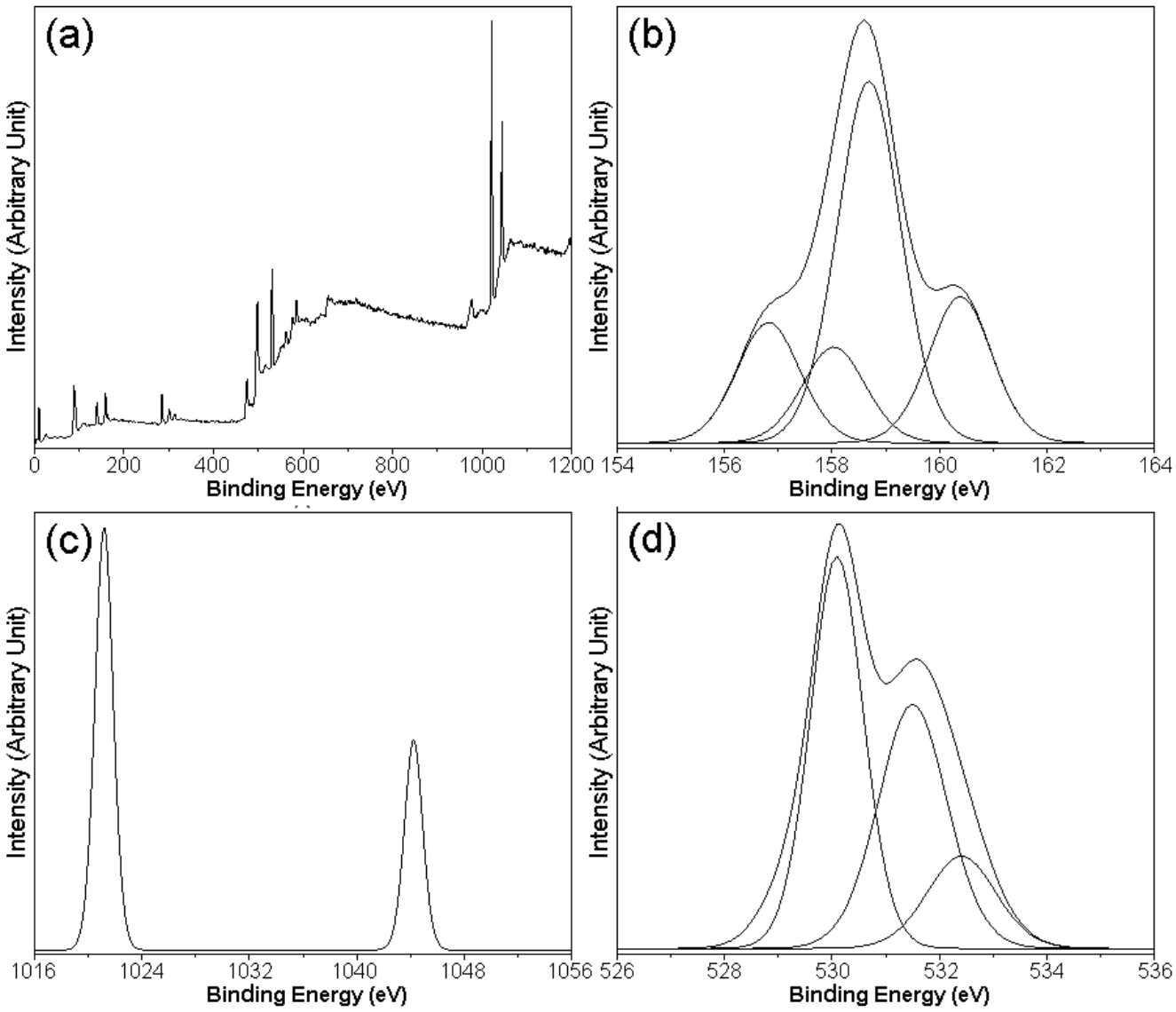

Fig. 4. (a) XPS survey spectrum and (b–d) high-resolution XPS spectra of Y 3d, Zn 2p and O 1s of 3% Y-doped ZnO, respectively.

The optical property of ZnO with and without Y dopant was investigated by UV-Visible spectroscopy as the result shown in Fig. 6. The pure ZnO and Y-doped ZnO samples showed excellent UV absorption with the maximum absorption at 367 nm for ZnO and 374 nm for 5% Y-doped ZnO which is typically associated with charge transfer process from valence band to conduction band [2,4,6,8,16]. Moreover, the maximum absorption of Y-doped ZnO was red-shifted due to the formation of shallow level inside band gap caused by impurity containing in the lattice [4,6,43,44]. The energy gap was calculated using the equation: E_g (eV) = 1,240/λ_g. The band gap of sample was decreased from 3.37 eV for ZnO to 3.31 eV for 5% Y-doped ZnO, indicating that Y dopant played the role in influencing the band gap of ZnO which is the benefit to enhance the photocatalytic activity of ZnO under visible light irradiation [2,4,6,43,44].

The MB as a dye model was selected to investigate the photocatalytic activity of the as-synthesized ZnO and Y-doped ZnO samples under visible light irradiation. Fig. 7 shows the absorption spectra of MB in the presence of ZnO and Y-doped ZnO nanoparticles under visible light irradiation for different lengths of irradiation time. Clearly, the intensity at maximum absorption wavelength of MB was deceased with increasing in the irradiation time from 0 to 100 min. In this research, the 3% Y-doped ZnO nanoparticles show the decrease of MB content faster than any other samples. The Y dopant played the role in degrading of MB dye photocatalyzed by ZnO nanoparticles under visible light irradiation.

Fig. 8a shows the degradation of MB photocatalyzed by pure ZnO and Y-doped ZnO nanoparticles illuminated by UV light. The Y-doped ZnO nanoparticles have the efficiency higher than un-doped ZnO nanoparticles. Among them, the 3% Y-doped ZnO nanoparticles show the highest photocatalytic activity. The photodegradation of MB were 20.16%, 78.58%, 97.19% and 92.34% for pure ZnO,

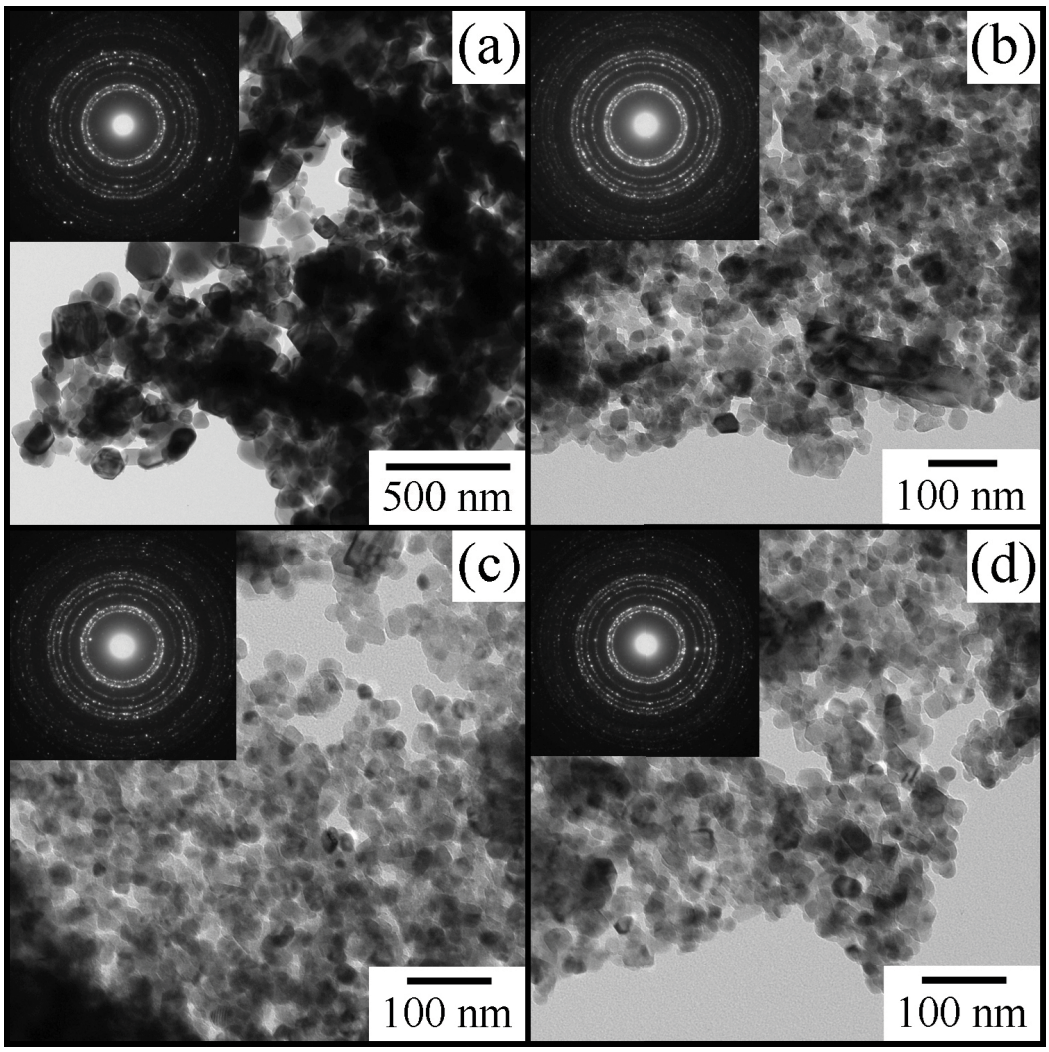

Fig. 5. TEM images and SAED patterns of the as-synthesized (a–d) 0%, 1%, 3% and 5% Y-doped ZnO samples, respectively.

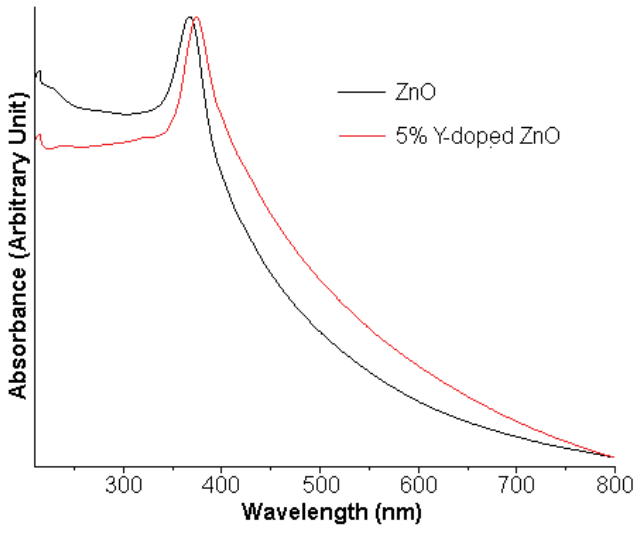

Fig. 6. UV-Visible absorption of ZnO and 5% Y-doped ZnO samples.

1% Y-doped ZnO, 3% Y-doped ZnO and 5% Y-doped ZnO nanoparticles, respectively. In particular, Y-doped ZnO nanoparticles absorbed photon which can lead to photo-excited electrons and photo-induced holes in conduction and valence bands of ZnO nanoparticles [2,5,6,9,29]. The Y^{3+} ion accepted the photo-excited electron and was transformed into Y^{2+} ion. The recombination of electron and hole was inhibited, the lifetime of electron and hole was lengthened, and the photocatalytic reaction was enhanced [5,6,9,29]. The Y^{2+} ion was oxidized by reacting with dissolved O_2 to generate $^{\bullet}O_2^-$ radical while the photo-induced hole at valence band diffused to surface of Y-doped ZnO nanoparticles and reacted with OH^-/H_2O to produce $^{\bullet}OH$ radical [5,6,9,29]. The $^{\bullet}O_2^-$ and $^{\bullet}OH$ radicals played the role in degrading of MB to final products [5,6,8,9,29]. Fig. 8b shows the plot of $\ln(C_o/C_t)$ vs. time for the degradation of MB photocatalyzed by ZnO and Y-doped ZnO nanoparticles under visible light irradiation. The photodegradation kinetics of MB over ZnO and Y-doped ZnO nanoparticles can be calculated by the Langmuir–Hinshelwood kinetic model [6,15,25,29]. For the linear graph with $R^2 > 0.95$, the kinetic

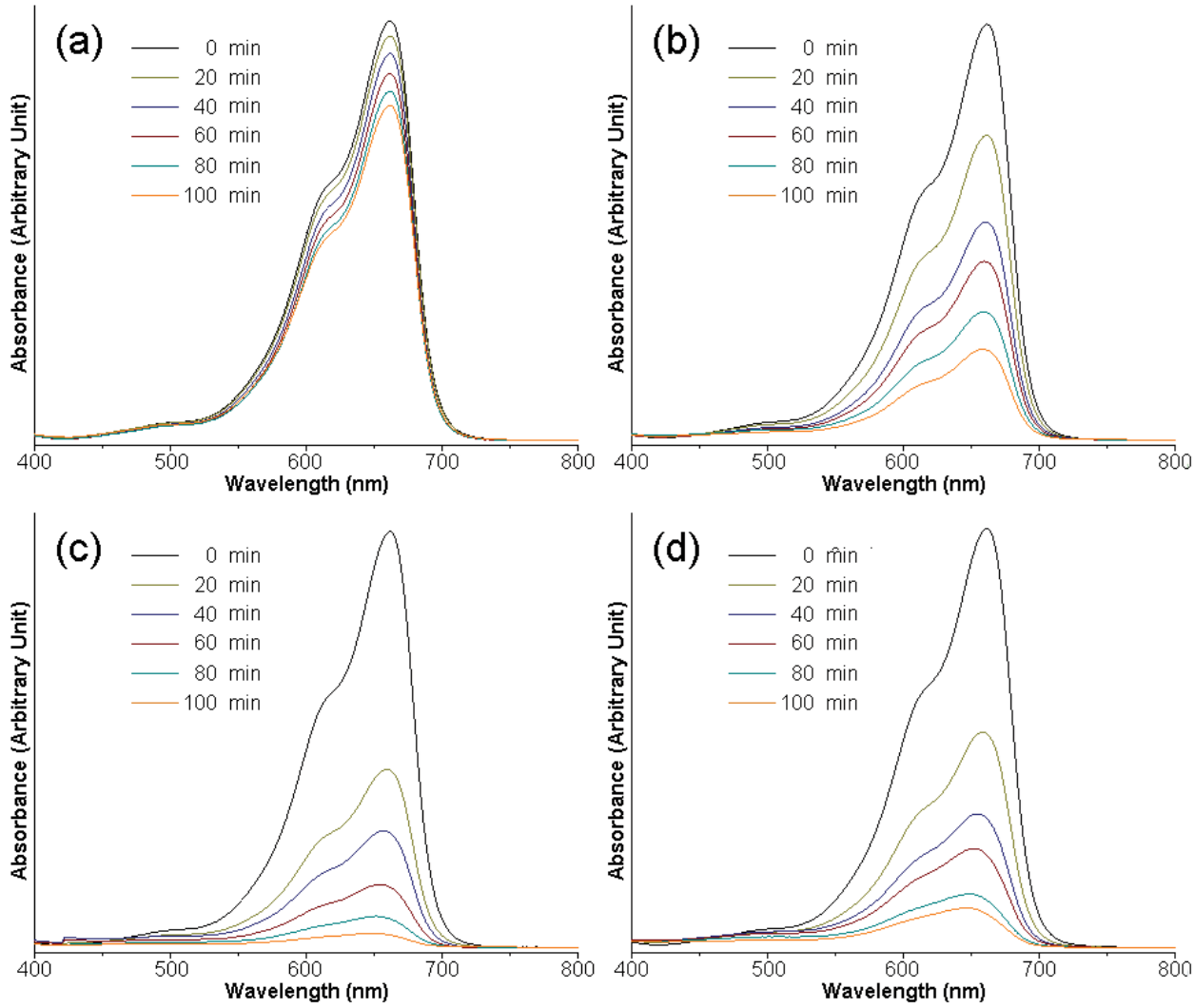

Fig. 7. UV-Visible absorption of MB solutions photocatalyzed by (a–d) 0%, 1%, 3% and 5% Y-doped ZnO nanoparticles under visible radiation, respectively.

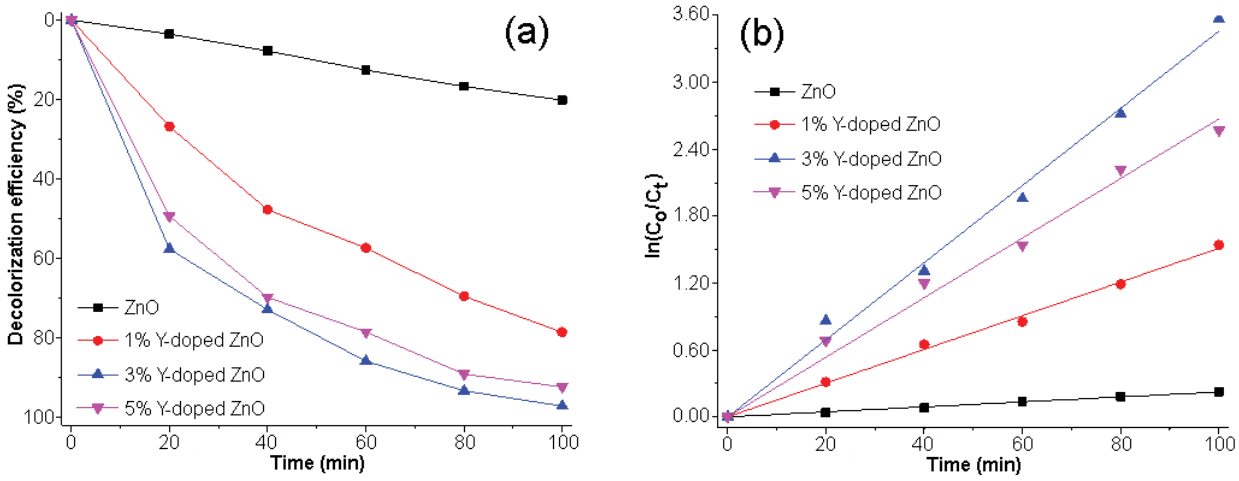

Fig. 8. (a) Decolorization efficiencies and (b) reaction kinetics for photodegradation of MB by 0%–5% Y-doped ZnO nanoparticles induced by visible radiation.

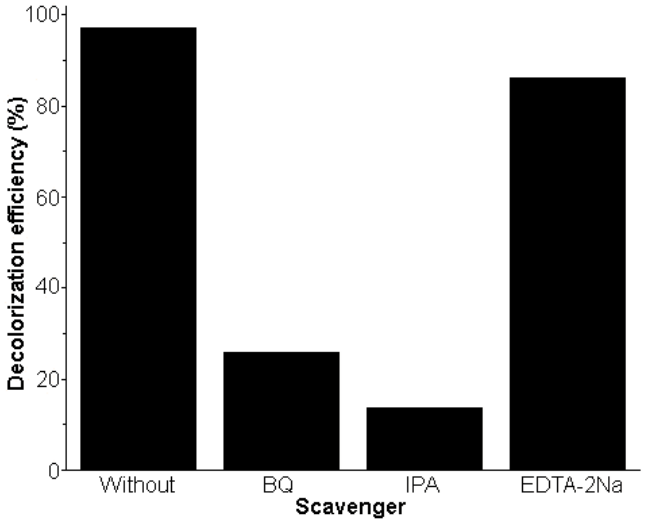

Fig. 9. Effect of different scavengers on the degradation of MB photocatalyzed by 3% Y-doped ZnO nanoparticles under visible radiation.

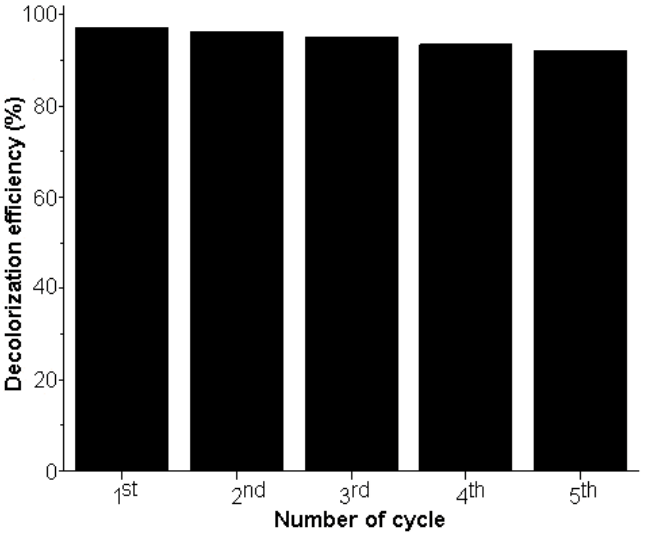

Fig. 10. Stability and recyclability of the reused 3% Y-doped ZnO nanoparticles illuminated by visible light within five cycles.

reaction of MB degradation over photocatalyst is the pseudo-first-order kinetic model [6,13,15]. The rate constants of MB degradation over photocatalyst were 2.20×10^{-3}, 0.0152, 0.0346 and 0.0267 min^{-1} for pure ZnO, 1% Y-doped ZnO, 3% Y-doped ZnO and 5% Y-doped ZnO, respectively. Particularly, the 3% Y-doped ZnO nanoparticles have the highest rate constant for MB degradation. The rate constant of 3% Y-doped ZnO nanoparticles is 15.73 times that of pure ZnO nanoparticles. Y ion, an electron donor, reacted with adsorbed oxygen and led to prevent electron–hole recombination [6,32]. In addition, the active species for MB degradation photocatalyzed by Y-doped ZnO nanoparticles was investigated by the use of ethylenediaminetetraacetic acid disodium salt (EDTA-2Na), isopropyl alcohol (IPA)

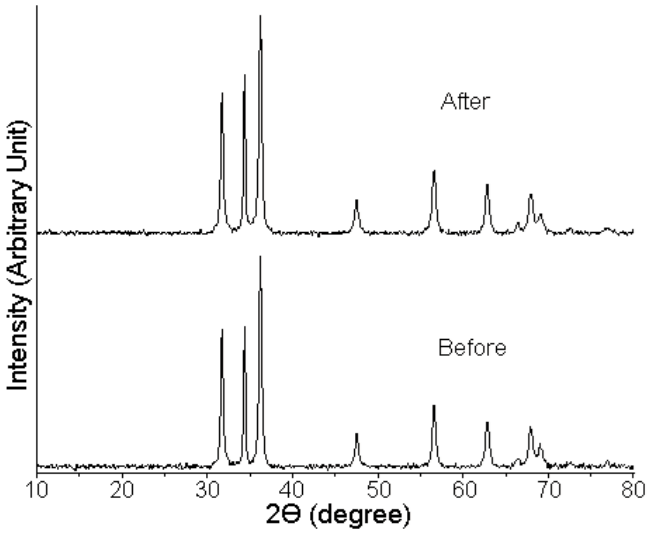

Fig. 11. XRD patterns of 3% Y-doped ZnO nanoparticles before and after photocatalytic reaction within five cycles.

and benzoquinone (BQ) as the scavengers of h^+, $^{\bullet}OH$ and $^{\bullet}O_2^-$ (Fig. 9) [13,45,46]. When EDTA-2Na, IPA and BQ were added in the photocatalytic reactor, the photodegradation efficiencies were deceased to 86.23%, 13.75% and 25.78%, respectively. Clearly, $^{\bullet}OH$ and $^{\bullet}O_2^-$ radicals are main active species for MB degradation over Y-doped ZnO nanoparticles under visible light irradiation.

The photostability and reusability of 3% Y-doped ZnO nanoparticles were tested under visible light irradiation (Fig. 10). At the end of five recycles, the efficiency in degrading of MB photocatalyzed by 3% Y-doped ZnO nanoparticles was reduced to 92.15%. Thus, the 3% Y-doped ZnO nanoparticles were stable enough for practical application. Furthermore, the phase and structure of reused 3% Y-doped ZnO nanoparticles at the end of the 5th recycle was analyzed by XRD (Fig. 11). It can be classified as hexagonal wurtzite structure of ZnO in agreement to the JCPDS No. 36-1451. The result indicated that the 3% Y-doped ZnO nanoparticles were excellent photo-corrosion resistance and stable for practical application under visible light irradiation.

4. Conclusions

In summary, Y-doped ZnO nanoparticles as visible-light driven photocatalyst were successfully synthesized by a tartaric acid-assisted combustion method. All samples can be indexed to the pure phase of hexagonal wurtzite ZnO nanoparticles with the sizes of 72.91 ± 24.68 nm, 24.05 ± 7.24 nm, 21.83 ± 4.90 nm and 21.55 ± 3.81 nm for pure ZnO, 1% Y-doped ZnO, 3% Y-doped ZnO and 5% Y-doped ZnO, respectively. The 3% Y-doped ZnO nanoparticles exhibited the highest MB degradation under visible light irradiation because Y^{3+} ions as electron acceptors played the role in inhibiting the recombination of electrons and holes and enhancing the photocatalytic reaction. In this research, 3% Y-doped ZnO nanoparticles were excellent photo-corrosion resistance and have stability for practical application under visible light irradiation.

Declaration of competing interest

The authors declare that they have no known competing financial interests or personal relationships that could have appeared to influence the work reported in this paper.

Acknowledgements

This research was supported by National Science, Research and Innovation Fund (NSRF) and Prince of Songkla University (Grant No. SCI6601194S).

References

[1] E. Luévano-Hipólito, A.M. Cruz, Sol–gel synthesis and photocatalytic performance of ZnO toward oxidation reaction of NO, Res. Chem. Intermed., 42 (2016) 4879–4891.
[2] Z. Barzgari, A. Ghazizadeh, S.Z. Askari, Preparation of Mn-doped ZnO nanostructured for photocatalytic degradation of orange G under solar light, Res. Chem. Intermed., 42 (2016) 4303–4315.
[3] R. Jeyachitra, V. Senthilnathan, T.S. Senthil, Studies on electrical behavior of Fe doped ZnO nanoparticles prepared via co-precipitation approach for photo-catalytic application, J. Mater. Sci., 29 (2018) 1189–1197.
[4] K.P. Raj, K. Sadaiyandi, A. Kennedy, S. Sagadevan, Photocatalytic and antibacterial studies of indium-doped ZnO nanoparticles synthesized by co-precipitation technique, J. Mater. Sci., 28 (2017) 19025–19037.
[5] A. Rahman, R. Jayaganthan, Synthesis, characterization and photocatalytic studies of La, Dy-doped ZnO nanoparticles, Trans. Indian Inst. Met., 70 (2017) 1063–1074.
[6] G. Vijayaprasath, P. Soundarrajan, G. Ravi, Synthesis of ZnO nanosheets morphology by Ce doping for photocatalytic activity, J. Electron. Mater., 48 (2019) 684–695.
[7] M. Rafique, R. Tahir, N.R. Khalid, M.B. Tahir, M. Irshad, S.S.A. Gillani, A. Usman, K. Shahzad, A.M. Ali, S. Muhammad, Hydrothermal synthesis of an efficient and visible light responsive pure and strontium doped zinc oxide nano-hexagonal photocatalysts for photodegradation of rhodamine B dye, Appl. Nanosci., 11 (2021) 1045–1056.
[8] R. Khan, S. Raj, J.H. Yun, Y.T. Yu, J.I. Lee, I.H. Lee, Facile preparation of ZnO nanosheets and its photocatalytic activity in the degradation of rhodamine B dye under UV irradiation, Electron. Mater. Lett., 12 (2016) 784–788.
[9] I. Ahmad, M.S. Akhtar, E. Ahmed, M. Ahmad, Facile synthesis of Pr-doped ZnO photocatalyst using sol–gel method and its visible light photocatalytic activity, J. Mater. Sci., 31 (2020) 1084–1093.
[10] M.S. Nasrollahzadeh, M. Hadavifar, S.S. Ghasemi, M.A. Chamjangali, Synthesis of ZnO nanostructure using activated carbon for photocatalytic degradation of methyl orange from aqueous solutions, Appl. Water Sci., 8 (2018) 104, doi: 10.1007/s13201-018-0750-6.
[11] M.M. Ba-Abbad, M.S. Takriff, A.W. Mohammad, Enhancement of 2-chlorophenol photocatalytic degradation in the presence Co^{2+}-doped ZnO nanoparticles under direct solar radiation, Res. Chem. Intermed., 42 (2016) 5219–5236.
[12] S.G. Kumar, K.S.R.K. Rao, Zinc oxide based photocatalysis: tailoring surface-bulk structure and related interfacial charge carrier dynamics for better environmental applications, RSC Adv., 5 (2015) 3306–3351.
[13] A. Phuruangrat, B. Kuntalue, S. Thongtem, T. Thongtem, Hydrothermal synthesis of hexagonal ZnO nanoplates used for photodegradation of methylene blue, Optik, 226 (2021) 165949, doi: 10.1016/j.ijleo.2020.165949.
[14] H.-Y. Lee, C.-Y. Cheng, C.-T. Lee, Bottom gate thin-film transistors using parallelly lateral ZnO nanorods grown by hydrothermal method, Mater. Sci. Semicond. Process., 119 (2020) 105223, doi: 10.1016/j.mssp.2020.105223.
[15] S. Sa-nguanprang, A. Phuruangrat, T. Thongtem, S. Thongtem, Synthesis of ZnO nanoparticles by tartaric acid solution combustion and their photocatalytic properties, Russ. J. Inorg. Chem., 65 (2020) 1102–1110.
[16] D. Thakur, A. Sharma, D.S. Rana, N. Thakur, D. Singh, T. Tamulevicius, M. Andrulevicius, S. Tamulevicius, S.K. Shukla, S. Thakur, Facile synthesis of silver-doped zinc oxide nanostructures as efficient scaffolds for detection of p-nitrophenol, Chemosensors, 8 (2020) 108, doi: 10.3390/chemosensors8040108.
[17] X. Lian, Y. Li, T. Lv, Y. Zou, D. An, N. Zhang, Preparation of ZnO nanoparticles by combustion method and their gas sensing properties, Electron. Mater. Lett., 12 (2016) 24–31.
[18] K.R. Ahammed, Md. Ashaduzzaman, S.C. Paul, M.R. Nath, S. Bhowmik, O. Saha, Md.M. Rahaman, S. Bhowmik, T.D. Aka, Microwave assisted synthesis of zinc oxide (ZnO) nanoparticles in a noble approach: utilization for antibacterial and photocatalytic activity, SN Appl. Sci., 2 (2020) 955, doi: 10.1007/s42452-020-2762-8.
[19] A. Phuruangrat, T. Thongtem, B. Kuntalue, S. Thongtem, Microwave-assisted synthesis and characterization of rose-like and flower-like zinc oxide nanostructures, J. Ovonic Res., 7 (2011) 107–113.
[20] S.K. Chawla, P. Kaur, R.K. Mudsainiyan, S.S. Meena, S.M. Yusuf, Effect of fuel on the synthesis, structural, and magnetic properties of M-type hexagonal $SrFe_{12}O_{19}$ nanoparticles, J. Supercond. Novel Magn., 28 (2015) 1589–1599.
[21] S. Sasikumar, R. Vijayaraghavan, Effect of metal-ion-to-fuel ratio on the phase formation of bioceramic phosphates synthesized by self-propagating combustion, Sci. Technol. Adv. Mater., 9 (2008) 035003, doi: 10.1088/1468-6996/9/3/035003.
[22] I.T. Papadas, A. Ioakeimidis, G.S. Armatas, S.A. Choulis, Low-temperature combustion synthesis of a spinel $NiCo_2O_4$ hole transport layer for perovskite photovoltaics, Adv. Sci., 5 (2018) 1701029, doi: 10.1002/advs.201701029.
[23] G. Clarke, A. Rogov, S. McCarthy, L. Bonacina, Y. Guńko, C. Galez, R.L. Dantec, Y. Volkov, Y. Mugnier, A. Prina-Mello, Preparation from a revisited wet chemical route of phase-pure, monocrystalline and SHG-efficient $BiFeO_3$ nanoparticles for harmonic bio-imaging, Sci. Rep., 8 (2018) 10473, doi: 10.1038/s41598-018-28557-w.
[24] H. Vahdat Vasei, S.M. Masoudpanah, M. Adeli, M.R. Aboutalebi, Photocatalytic properties of solution combustion synthesized ZnO powders using mixture of CTAB and glycine and citric acid fuels, Adv. Powder Technol., 30 (2019) 284–291.
[25] Powder Diffract. File, JCPDS-ICDD, 12 Campus Boulevard, Newtown Square, PA 19073–3273, USA, 2001.
[26] D.J. Kim, S.H. Hyun, S.G. Kim, M. Yashima, Effective ionic radius of Y^{3+} determined from lattice parameters of fluorite-type HfO_2 and ZrO_2 solid solutions, J. Am. Ceram. Soc., 77 (1994) 597–599.
[27] Y. Hiroshi, K. Eiji, I. Ichikawa, K. Katsuyoshi, M. Toshiyuki, H. Hajime, Multiple doping effect on the electrical conductivity in the $(Ce_{1-x-y}La_xM_y)O_{2-\delta}$ (M = Ca, Sr) system, Electrochemistry, 68 (2000) 455–459.
[28] H. Yang, L. Jun, B. Han, S. Zhenjia, W. Ming, Z. Zhongxiang, Effect of octahedron tilt on the structure and magnetic properties of bismuth ferrite, J. Adv. Ceram., 9 (2020) 641–646.
[29] A. Phuruangrat, T. Thongtem, S. Satchawan, S. Thongtem, Photocatalytic activity of rugby-like Nd-doped ZnO particles activated by ultraviolet, Dig. J. Nanomater. Biostruct., 13 (2018) 625–630.
[30] S. Sitthichai, A. Phuruangrat, T. Thongtem, S. Thongtem, Influence of Mg dopant on photocatalytic properties of Mg-doped ZnO nanoparticles prepared by sol–gel method, J. Ceram. Soc. Jpn., 125 (2017) 122–124.
[31] K.-S. Yu, J.-Y. Shi, Z.-L. Zhang, Y.-M. Liang, W. Liu, Synthesis, characterization, and photocatalysis of ZnO and Er-doped ZnO, J. Nanomater., 2013 (2013) 372951, doi: 10.1155/2013/372951.
[32] H. Parangusan, D. Ponnamma, M.A.A. Al-Maadeed, A. Marimuthu, Nanoflower-like yttrium-doped ZnO photocatalyst for the degradation of methylene blue dye, Photochem. Photobiol., 94 (2018) 237–246.

[33] A.F. Abdulrahman, Study the optical properties of the various deposition solutions of ZnO nanorods grown on glass substrate using chemical bath deposition technique, J. Ovonic Res., 16 (2020) 181–188.
[34] S. Guo, Z. Du, S. Dai, Analysis of Raman modes in Mn-doped ZnO nanocrystals, Phys. Status Solidi B, 246 (2009) 2329–2332.
[35] Z.A. Abdelouhab, D. Djouadi, A. Chelouche, T. Touam, Structural, morphological and Raman scattering studies of pure and Ce-doped ZnO nanostructures elaborated by hydrothermal route using nonorganic precursor, J. Sol-Gel Sci. Technol., 95 (2020) 136–145.
[36] M. Mazhdi, M.J. Tafreshi, The effects of gadolinium doping on the structural, morphological, optical, and photoluminescence properties of zinc oxide nanoparticles prepared by co-precipitation method, Appl. Phys. A, 124 (2018) 863, doi: 10.1007/s00339-018-2291-0.
[37] M. Faraz, M.Z. Ansari, N. Khare, Synthesis of nanostructure manganese doped zinc oxide/polystyrene thin films with excellent stability, transparency and superhydrophobicity, Mater. Chem. Phys., 211 (2018) 137–143.
[38] T.L. Tan, C.W. Lai, S.B.A. Hamid, Tunable band gap energy of Mn-doped ZnO nanoparticles using the coprecipitation technique, J. Nanomater., 2014 (2014) 371720, doi: 10.1155/2014/371720.
[39] L. Cheng, S.Y. Ma, X.B. Li, J. Luo, W.Q. Li, F.M. Li, Y.Z. Mao, T.T. Wang, Y.F. Li, Highly sensitive acetone sensors based on Y-doped SnO_2 prismatic hollow nanofibers synthesized by electrospinning, Sens. Actuators, B, 200 (2014) 181–190.
[40] S.M. Suturin, A.M. Korovin, V.E. Bursian, L.V. Lutsev, V. Bourobina, N.L. Yakovlev, M. Montecchi, L. Pasquali, V. Ukleev, A. Vorobiev, A. Devishvili, N.S. Sokolov, Role of gallium diffusion in the formation of a magnetically dead layer at the $Y_3Fe_5O_{12}/Gd_3Ga_5O_{12}$ epitaxial interface, Phys. Rev. Mater., 2 (2018) 104404.
[41] Y.C. Cao, L. Zhao, J. Luo, K. Wang, B.P. Zhang, H. Yokota, Y. Ito, J.F. Li, Plasma etching behavior of Y_2O_3 ceramics: comparative study with Al_2O_3, Appl. Surf. Sci., 366 (2016) 304–309.
[42] L. Mai, N. Boysen, E. Subas, T. Arcos, D. Rogalla, G. Grundmeier, C. Bock, H.L. Lu, A. Devi, Water assisted atomic layer deposition of yttrium oxide using tris(N,N_0-diisopropyl-2-dimethylamido-guanidinato) yttrium(III): process development, film characterization and functional properties, RSC Adv., 8 (2018) 4987–4994.
[43] T.B. Ivetić, M.R. Dimitrievska, I.O. Gúth, Lj.R. Dačanin, S.R. Lukić-Petrović, Structural and optical properties of europium-doped zinc oxide nanopowders prepared by mechanochemical and combustion reaction methods, J. Res. Phys., 36 (2012) 43–51.
[44] H. Chemingui, J.C. Mzali, T. Missaoui, M. Konyar, M. Smiri, H.C. Yatmaz, A. Hafiane, Characteristics of Er-doped zinc oxide layer: application in synthetic dye solution color removal, Desal. Water Treat., 209 (2021) 402–413.
[45] N. Duraisamy, K. Kandiah, R. Rajendran, S. Prabhu, R. Ramesh, G. Dhanaraj, Electrochemical and photocatalytic investigation of nickel oxide for energy storage and wastewater treatment, Res. Chem. Intermed., 44 (2018) 5653–5667.
[46] Z. Jiao, Z. Liu, Z. Ma, Rodlike AgI/$Ag_2Mo_2O_7$ heterojunctions with enhanced visible-light-driven photocatalytic activity, ACS Omega, 4 (2019) 7919–7930.